Grid of pseudo-2D chemistry models for tidally locked exoplanets – II. The role of photochemistry

Robin Baeyens,[1][*] Thomas Konings,[1] Olivia Venot,[2] Ludmila Carone[3,4] and Leen Decin[1]

[1]*Institute of Astronomy, KU Leuven, Celestijnenlaan 200D, 3001 Leuven, Belgium*
[2]*Université de Paris and Université Paris-Est Créteil, CNRS, LISA, F-75013 Paris, France*
[3]*Max-Planck-Institut für Astronomie, Königstuhl 17, 69117 Heidelberg, Germany*
[4]*Centre for Exoplanet Science, School of Physics & Astronomy, University of St Andrews, North Haugh, St Andrews, KY169SS, UK*

ABSTRACT

Photochemistry is expected to change the chemical composition of the upper atmospheres of irradiated exoplanets through the dissociation of species, such as methane and ammonia, and the association of others, such as hydrogen cyanide. Although primarily the high altitude day side should be affected by photochemistry, it is still unclear how dynamical processes transport photochemical species throughout the atmosphere, and how these chemical disequilibrium effects scale with different parameters. In this work we investigate the influence of photochemistry in a two-dimensional context, by synthesizing a grid of photochemical models across a large range of temperatures. We find that photochemistry can strongly change the atmospheric composition, even up to depths of several bar in cool exoplanets. We further identify a sweet spot for the photochemical production of hydrogen cyanide and acetylene, two important haze precursors, between effective temperatures of 800 and 1400 K. The night sides of most cool planets ($T_{\rm eff}$ < 1800 K) are shown to host photochemistry products, transported from the day side by horizontal advection. Synthetic transmission spectra are only marginally affected by photochemistry, but we suggest that observational studies probing higher altitudes, such as high-resolution spectroscopy, take photochemistry into account.

Key words: planets and satellites: atmospheres – planets and satellites: composition – planets and satellites: gaseous planets.

1 INTRODUCTION

The day-side hemispheres of tidally locked exoplanets are constantly being irradiated by ultraviolet (UV) radiation originating from the stellar host. This irradiation in turn leads to photochemistry in the planet's atmosphere, by which we mean the set of chemical reactions and reaction mechanisms that incorporate interactions with a photon. In the Solar System planets, photochemistry is ubiquitous (e.g. Yung & DeMore 1999; Strobel 2005; Moses et al. 2020, and references therein). Because of their strong one-sided irradiation, gaseous tidally locked exoplanets are likewise expected to have their chemical composition, and their potential transmission signatures, altered by photochemistry. Indeed, effects of disequilibrium chemistry are just starting to be probed through exoplanet observations (Baxter et al. 2021; Roudier et al. 2021).

Another potential impact of photochemistry is the formation of hazes. Given the common detections of haze in exoplanetary atmospheres (e.g. Pont et al. 2008, 2013; Sing et al. 2016), photo-chemistry of long hydrocarbons has been proposed as a formation mechanism for these haze species, in analogy to the formation of hazes in the atmospheres of the Earth (Jacobson et al. 2000) and the Solar System giant planets (e.g. Yung et al. 1984; Gladstone et al. 1996; Moses et al. 2000; Wong et al. 2003). For this reason, photochemical models (Liang et al. 2004; Zahnle et al. 2009a, 2016; Kawashima & Ikoma 2018, 2019) and laboratory experiments (He et al. 2018; Hörst et al. 2018; Fleury et al. 2019, 2020; Yu et al. 2021) have specifically targeted the formation and evolution of hydrocarbon hazes via photochemistry.

Previous 1D photochemical studies of irradiated exoplanets found that the upper layers (p < 10^{-3} bar) of hot Jupiters can be strongly affected by photochemistry, in particular through the photolysis (i.e. dissociation after interaction with a photon) of molecules such as CH_4 and NH_3 (Zahnle et al. 2009a; Moses et al. 2011; Venot et al. 2012; Rimmer & Helling 2016; Drummond et al. 2016; Hobbs et al. 2019). The resulting large amounts of H (Liang et al. 2003) and other atomic components (Moses 2014) are then free to diffuse and recombine into different species, such as HCN and C_2H_2. Photochemical kinetics studies have demonstrated a greater effect

of photochemistry – and chemical disequilibrium in general – in exoplanets with lower effective temperatures, both because cooler atmospheres have slower chemical timescales, as well as high abundances of photochemically active species (Moses 2014). The above photochemistry findings, established with hot Jupiter models, are likewise supported by hydrogen-rich sub-Neptune models (Miller-Ricci Kempton et al. 2012; Moses et al. 2013b; Hu & Seager 2014; Miguel & Kaltenegger 2014). However, the relative importance of photochemistry varies with modelling choices such as the thermal profile (Venot et al. 2014), elemental composition (Line et al. 2011; Moses et al. 2013b), and vertical mixing efficiency (Agúndez et al. 2014b; Miguel & Kaltenegger 2014). Additionally, photochemical networks including sulfur have been used to infer relatively high abundances of H_2S and HS, as well as abundance discrepancies of non-sulfurous species relative to pure C/N/O/H networks (Zahnle et al. 2009b; Hobbs et al. 2021; Hu 2021; Tsai et al. 2021). Other studies, still, have focused on the uppermost layers of the atmosphere, including ion photochemistry (Yelle 2004; García Muñoz 2007; Koskinen et al. 2013; Lavvas et al. 2014; Rimmer & Helling 2016; Helling & Rimmer 2019; Barth et al. 2021; Locci et al. 2022). Connecting the different physical regimes in the upper and lower atmospheres of exoplanets is still an active topic of research.

Given the unique day-night dichotomy of tidally locked exoplanets, several two-dimensional (Agúndez et al. 2014a; Venot et al. 2020b; Moses et al. 2021; Baeyens et al. 2021) and three-dimensional (Cooper & Showman 2006; Mendonça et al. 2018; Steinrueck et al. 2019; Drummond et al. 2018a,b,c, 2020) models have been employed to investigate the spatial variations in the atmospheric chemistry of exoplanets. These studies have demonstrated the potential of efficient zonal (and meridional, Drummond et al. 2018c, 2020) advection to remove longitudinal chemical variations, primarily in cooler planets (Baeyens et al. 2021). The averaged chemical composition is then mostly similar to that of the day side. However, because of the computational cost of 3D chemistry-coupled GCMs, most studies have relied on parametrized chemistry rather than chemical kinetics, and as such have not included photochemistry. The pseudo-2D studies that did include photochemical reactions (Agúndez et al. 2014a; Venot et al. 2020b; Moses et al. 2021) have found zonal variations down to 10^{-4} bar due to photodissociation, and a potentially large photochemical production of HCN. Vigorous atmospheric mixing processes transport photodissociated day-side species to deeper layers, or to the night side of the planet, where they recombine. Cool planets with $T_{\rm eff} = 500 - 700$ K potentially experience the strongest impact of photochemistry (Moses et al. 2021).

The parameter space for photochemistry is nevertheless largely unexplored in a 2D context. Moses et al. (2021) have varied the effective temperature and metallicity of photochemical models, but they did not explicitly investigate the impact of the host star. The stellar spectrum, size, and distance, all influence the UV flux impinging on the planetary atmosphere and the strength of photochemical processes. Moreover, it remains unclear in which planets photochemistry could affect also the middle, photospheric region of the atmosphere ($\sim$1–100 mbar), where it could play a role in the formation of infrared transmission features.

In this paper, we aim to find out which planets experience large effects of photochemistry impacting their atmospheric composition, and which planets do not. To this end, we build upon the grid of pseudo-2D chemistry models developed in Baeyens et al. (2021), by incorporating photochemical reactions, in addition to the previously included processes of vertical and horizontal mixing. We further synthesize transmission spectra for each model, estimating the extent to which photochemistry modifies the observations.

The outline of this paper is as follows. In Section 2, the chemical kinetics code and the framework of the model grid are presented. Since we build upon the results of Baeyens et al. (2021), we focus mostly on describing the implementation of photochemistry. The new photochemical models are presented in Section 3, and discussed in a broader context in Section 4. Specifically, we focus on whether photochemistry affects the deep atmosphere or the night side (Section 4.1). We also discuss the impact of a hot thermosphere (Section 4.2), a comparison to past photochemical models (Section 4.3), and possible implications for high-resolution spectroscopy (Section 4.4) and hazes (Section 4.5). Finally, our conclusions are presented in Section 5.

2   MODELLING TOOLS

The chemical models are computed with the pseudo-2D chemical kinetics code developed by Agúndez et al. (2014a), which includes disequilibrium chemistry via vertical mixing (K_{zz}), horizontal advection and photochemical reactions. We compute our grid of photochemical models in largely the same way as described in Baeyens et al. (2021), namely by post-processing the outcomes of a 3D GCM grid with the chemical kinetics code. However, the inclusion of photochemistry requires some changes to the modelling setup, which are detailed below.

As in Baeyens et al. (2021), we assume a solar elemental composition, which implies a C/O ratio of 0.55. The pseudo-2D code is initialized with a fully converged, one-dimensional photochemical kinetics model, corresponding to the substellar point. It is then integrated for a total of 50 rotations, so that a periodic steady-state can be reached.

2.1   Upper Atmosphere Extension

Because photochemistry mainly occurs in the upper atmosphere, we have extended the pressure domain of the simulation from 10^{-4} bar (Baeyens et al. 2021) to 10^{-8} bar. For some cold models, an upper boundary of 10^{-7} bar was chosen to avoid numerical issues. Although a 10^{-8}–10^{-7} bar upper boundary pressure is not unusual for chemical kinetics models (e.g. Agúndez et al. 2014a; Venot et al. 2020b; Moses et al. 2021), it is not a conservative choice, since it reaches well into the outer regions of the planet's atmosphere.[1] Accordingly, we have increased the number of vertical layers in the chemical model from 45 to up to 120.

The GCM models in our grid did not reach the low pressures up to 10^{-8} bar, so assumptions have been made to extrapolate the temperature- and K_{zz}-profiles, needed for the chemistry code, from 10^{-4} bar upward. Analytic calculations (Guillot 2010) and GCM simulations (e.g. Fig. 4, Baeyens et al. 2021) alike suggest that the temperature becomes approximately isothermal at pressures below 10^{-2} bar. Therefore, we have taken the simplest approach: to extend the temperature profiles isothermally upward from their value at 10^{-4} bar. It should nevertheless be noted that thermospheric models predict a strong temperature increase at pressures of $p < 10^{-6}$ bar (Yelle 2004; García Muñoz 2007; Koskinen et al. 2013), challenging

---

[1] For comparison, in the Earth's atmosphere, a pressure of 10^{-8} bar is attained at altitudes between 100 and 150 km (COESA 1976). This is above the Kármán line of 100 km, the conventional boundary for outer space.

the isothermal assumption made here. However, since we are mostly concerned with the impact of photochemistry on the atmospheric layers around 10–100 mbar that are probed with transmission spectroscopy, our isothermal extension should be sufficiently accurate. Still, the potential influence of thermospheric heating on our photochemical models is examined in Section 4.2.

Analogously, because we cannot derive the eddy diffusion coefficient at high altitudes from a GCM simulation, we simply adopt the value of K_{zz} at 10^{-4} bar (see Fig. 7, Baeyens et al. 2021) for lower pressures as well. Although K_{zz} generally increases with height (Parmentier et al. 2013; Komacek et al. 2019; Baeyens et al. 2021), it is expected to reach approximately constant values in the upper atmosphere (Steinrueck et al. 2021; Moses et al. 2021, and references therein). Given the uncertainties to this parameter, we opt again for a simple approach in all models. Finally, a molecular diffusive term is also included in the model, although it is not expected to play an important role at pressures greater than 10^{-8} bar (Venot et al. 2012).

2.2 Photochemical Network

Another difference between the models computed in this work and the models presented in Baeyens et al. (2021), is the chemical network. Here, we exchanged the reduced chemical network of Venot et al. (2020a) for the full network. Using the full network of Venot et al. (2020a) is required when including photochemistry, because the reduced network does not include photolysis reactions, nor is it optimized to accurately represent the upper atmosphere when photochemically active species are included. As such, the network we use here is the full network of Venot et al. (2020a), which includes 108 chemical species consisting of C, N, O, H, with 1906 reactions (948 of which are reversible, and 10 irreversible). The network also contains 52 photolysis reactions.

The photoabsorbing species are H_2O, CO_2, H_2CO, OH, OOH, H_2O_2, CO, H_2, HCO, CH_3OH, CH_3OOH, CH_2CO, CH_3CHO, CH_3, CH_4, C_2H, C_2H_2, C_2H_3, C_2H_4, C_2H_6, N_2, NH_2, NH_3, N_2H_4, HCN, H_2CN, C_2N_2, NO, NO_2, NO_3, HNO_2, HNO_3, N_2O, N_2O_4, and N_2O_3. For each of these species, wavelength-dependent cross-sections and quantum yields are used to determine the probability of a molecule absorbing a photon, and the fraction of such absorption events that result in molecular dissociation. For many reactions, multiple dissociation pathways are possible. Almost all photoabsorption cross-sections reside in the (X)UV domain and fall off quickly for wavelengths larger than 200 nm (Fig. 1). Some species have cross-sections that reach into the blue visible light, and three of them (HCO, NO_2, and NO_3) absorb in the full visible wavelength range. The photochemical data consist of mixed laboratory measurements and theoretical calculations, and are described in detail in Venot et al. (2012); Hébrard et al. (2013) and Dobrijevic et al. (2014). Although photochemical cross-sections are known to be temperature dependent (e.g. Venot et al. 2018, and references therein), the exact temperature-dependence is usually not well measured. Therefore, and since the effect of temperature-dependent cross-sections on transmission spectra is expected to be small (Venot et al. 2018), we do not take temperature-dependence of photochemical cross-sections into account here.

2.3 Stellar Spectra

To compute the photochemical dissociation rates, the incoming (UV) flux needs to be known. This quantity is provided via stellar spectral energy distributions, which are assumed to be constant
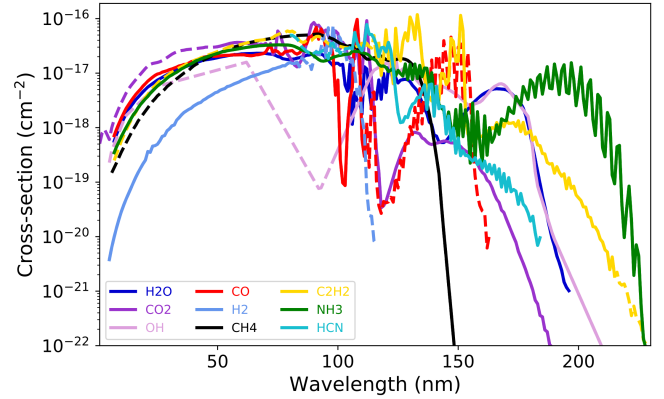
Figure 1. The photo-absorption (*dashed lines*) and photodissociation (*full lines*) cross-sections for a selection of abundant molecules in exoplanet atmospheres are highest in the UV wavelength range, and drop rapidly towards the visible wavelengths.
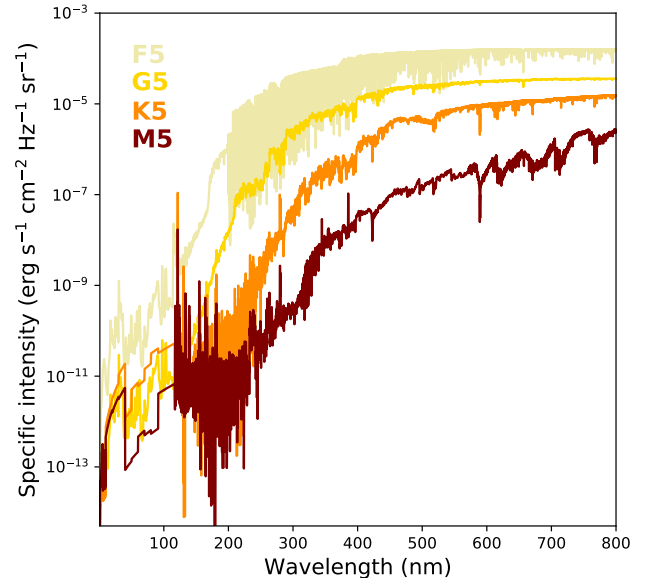
Figure 2. The spectral energy distributions (SEDs), used to compute the photodissociation rates, are shown for the different stellar types included in our grid.

in time. Given the framework of our grid, we adopt four spectral energy distributions ranging from 1 nm to 800 nm, which we apply for the M5, K5, G5, and F5 simulations (Fig. 2).

For the M- and K-star simulations, the spectral energy distributions are part of the *MUSCLES*[2] Treasury Survey (France et al. 2016; Youngblood et al. 2016; Loyd et al. 2016), a sample of panchromatic spectra for 11 low-mass exoplanet host stars that is made available via *MAST*[3]. These spectra are composed of PHOENIX stellar atmosphere models (Husser et al. 2013) in the visible wavelength range,


Hubble Space Telescope observations in the UV range (with spectral reconstructions of Lyman α and extreme UV (Youngblood et al. 2016)), and *Chandra* and *XMM-Newton* observations with plasma emission models (Smith et al. 2001) in the X-ray range. From this survey, we choose the star GJ 876 as a representative for the M5-star spectrum, and HD 85512 for the K5-spectrum (Fig. 2), since these two stars correspond well to the photospheric temperatures assumed in our grid (France et al. 2016). Flaring activity has been detected in the former star (Walkowicz et al. 2008; Poppenhaeger et al. 2010; France et al. 2012), but both spectral energy distributions have been constructed by making use of observations during low levels of activity (Loyd et al. 2016).

For the G5-star spectral energy distribution, we have adopted the present-day solar spectrum (Claire et al. 2012). The Sun provides a sufficiently close match to the 5650 K effective temperature of the paradigmatic G5-host star needed for our grid, with an excellent data quality (Fig. 2). However, it should be kept in mind that the present-day Sun is rather inactive compared to the stage when it was younger or to other G-type stars (e.g. Ribas et al. 2005), so the adopted spectrum again represents a reasonable lower limit on the UV flux.

For the F-type star, we have composed an F5-spectrum from different sources, due to a lack of spectral energy distributions covering the wavelength range from the X-ray regime to visible light. First, for the optical part up to 200 nm, again a PHOENIX model atmosphere is employed, with $T_{\rm eff}$ = 6500 K, log g = 4.5, and solar metallicity (Husser et al. 2013). In the UV range between 115 and 200 nm, we use the composite spectrum of the F-type star HD 128167, in units of flux, prepared by Segura et al. (2003) based on observations by the *International Ultraviolet Explorer* satellite. Finally, in the shortest wavelength range, between 1 and 115 nm, we have scaled the solar spectrum in such a way that the integrated luminosity in this bandwidth attains 10^{30} erg/s. This is a realistic value for F-stars, although luminosities between 10^{28} and 10^{31} erg/s seem possible (Panzera et al. 1999; Wang et al. 2020; Johnstone et al. 2021). For the luminosity scaling, a value of 1.35 $R_\odot$ was used as F5-star radius (Hubeny & Mihalas 2014). The resulting spectral energy distribution has the highest intensity of the four spectra used in this paper (Fig. 2).

Because most parameters in our atmospheric model grid are self-consistently coupled under the assumption of synchronous rotation, each model is at a different orbital distance from its host star (see Section 3 and Table 1 in Baeyens et al. 2021). The flux impinging on the top of the atmosphere depends on the stellar intensity, stellar radius and semi-major axis, and will thus also be different for each model. The stellar radii for each stellar type are adopted from Hubeny & Mihalas (2014) (their table 2.4) and equal 0.27, 0.68, 0.91, and 1.35 $R_\odot$ for the M5-, K5-, G5-, and F5-stars respectively. In order to compare the expected rate of photochemical dissociations between models, we have computed the UV irradiance at the top of the atmosphere of each model (Fig. 3). It appears that for the M-, K-, and G-type hosts, the distance-dependence of the planetary effective temperature approximately compensates for changes in the stellar luminosity, so that planets with the same effective temperature experience comparable UV irradiance. The planets with an F-type host, on the other hand, see a consistently higher UV flux for the same temperature, in line with their comparatively high UV intensity (Fig. 2).

Finally, we note that the chromospheric emission, and equivalently the UV flux, of stars is correlated with stellar activity, as well as stellar parameters such as age and rotation (Linsky et al. 2020). Therefore, the scatter among stars is large, and it is not a trivial
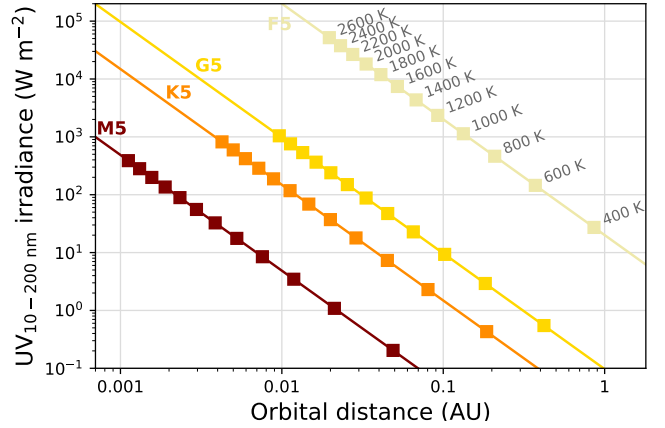
Figure 3. The UV irradiance as computed for the wavelength range between 10 nm to 200 nm, based on the four different stellar spectra shown in Fig. 2. The UV irradiance is plotted as a function of the orbital distance. The models of our grid are situated on the figure with squares. For a given planetary temperature, the M-, K-, and G-type stars give rise to comparable UV irradiance; the difference being a factor of a few. Given our choice of spectra, the planets orbiting F-type stars can be considered relatively highly irradiated.

exercise to typify the X-ray and UV spectrum of a certain stellar type, nor is it evident to capture the diversity in the observed stellar population. Even within the small *MUSCLES* sample, the estimated photodissociation rates can vary by an order of magnitude (Loyd et al. 2016). The scope of this work is to investigate the impact of photochemistry in a 2D-chemistry context for different planets. However, a future study investigating the chemical response to different parametrized stellar fluxes (cfr. Kawashima & Ikoma 2019) would be beneficial.

2.4 Model Runtimes

We briefly discuss the computational cost of taking into account photochemical reactions in the chemical kinetics code. To quickly reach model convergence, we adopted the same approach as laid out in Appendix A2 of Baeyens et al. (2021), which consists of initializing the code with a converged 1D chemical kinetics model at the substellar point. Since the vertical advection timescales are slower than those associated with photochemical dissociations, we did not notice a difference in the simulation time needed for convergence when photochemical reactions are included. We note that our similar runtimes for the cases with and without photochemistry should not necessarily be viewed as a general result, since the model setup and exact implementation of photochemical reactions in the kinetics model dictate the computation time.

Moreover, the necessary inclusion of a new chemical network with additional species and more reactions (Section 2.2) as well as an extension of the vertical grid (Section 2.1) lead to considerably longer runtimes when photochemistry is included. Specifically, a simulation making use of the full chemical network was recorded to run up to 80 times slower than a simulation with the reduced network. Thus, future studies would do well to balance the need for accurate photochemistry with the computational constraints introduced by using the complete chemical network, especially regarding the implementation in 2D or 3D models (e.g. Drummond et al. 2020).

3 SIMULATION RESULTS

3.1 Chemical Composition

Some of the most abundant molecular species, not counting H_2 and He, resulting from our pseudo-2D photochemical models with $g = 10$ m/s^2, are shown as a function of pressure at different longitudes (Fig. 4 for $T_{eff} = 400$–1400 K; Fig. 5 for $T_{eff} = 1600$–2600 K). The influence of photochemistry can clearly be seen, especially in the upper atmosphere ($p < 10^{-4}$ bar), where the chemical composition for all temperatures is characterized by rapid drops in the abundances of some species, as well as large variations with longitude. Furthermore, some photochemically active species, such as HCN, C_2H_2 or atomic hydrogen, display generally rising trends with altitude. Although the inclusion of photochemistry in our simulations modifies the chemical abundances strongly compared to a case with only mixing (Fig. 8 in Baeyens et al. 2021), the general conclusions that have been established using models without photochemistry remain valid.

On comparing the outcomes of our models to the chemistry simulations that did not include photochemistry (Fig. 8 in Baeyens et al. 2021), one can see that there is a good agreement in the abundances of species situated in the lower and middle atmospheres ($p > 1$ mbar). Chemical equilibrium and the quenching points are well reproduced, as we would indeed expect when switching between the reduced and full Venot et al. (2020a)-networks. The dominant molecules in the atmosphere, not taking into account H_2 and He, are still H_2O, supplemented by CH_4 in the cold atmospheres ($T_{eff} \lesssim 1000$ K) and by CO in the hot atmospheres ($T_{eff} \gtrsim 1000$ K). In the uppermost layers of the atmosphere ($p < 10^{-6}$ bar), however, photolysis of CH_4 and H_2O, can trigger CO production, making it the most abundant carbon-species at high altitudes even in cold atmospheres (e.g. at 600 K, Fig. 4). Moreover, in the 400 K F-host model it can even be seen that photochemically produced CO and CO_2 are mixed downward in sufficient quantities such that the overall tropospheric abundance is raised by an order of magnitude above the quenched abundance. This is evidenced by abrupt variations where the vertical profiles of CO and CO_2 connect to their respective quench points near 10 bar.

The dichotomy identified by Baeyens et al. (2021), in which cool atmospheres below 1400 K are zonally homogeneous, whereas warmer atmospheres are not, is still mostly valid, but only for pressures greater than 1 mbar. At lower pressures, photochemically driven day-night variations become noticeable, as the horizontal advection timescale is too slow to remove perturbations introduced by the increasing UV flux at the day side. Moreover, some photochemically produced species such as C_2H_2 or H vary zonally at even higher pressures.

An important consequence of the photodissociations of some species, is the increased amount of hydrogen cyanide (HCN) and acetylene (C_2H_2). Acetylene is more abundant in cool atmospheres, where it can reach a mixing ratio of 10^{-7} in the middle part (~10 mbar) and of 10^{-4} in the upper part (10^{-4} bar) of the atmosphere. In simulations with $T_{eff} > 1400$ K, the acetylene abundance drops quickly, together with that of methane. HCN reaches even higher abundances in the middle atmosphere, up to 10^{-6}, as it is produced at altitudes above the quenching point from dissociated ammonia and methane, according to the net reaction $NH_3 + CH_4 \rightarrow HCN + 3H_2$ (Moses 2014). At higher temperatures, the quenching points of HCN and its parent species shift to lower pressures, resulting in a lower abundance in the mid-atmospheric region (~1–100 mbar). In the upper regions, even for hotter cases, appreciable day-side quantities of HCN can potentially be retained (Fig. 5).

A sweet spot for photochemistry, exemplified by high abundances of HCN and C_2H_2 and photolysis of CH_4 and NH_3, appears to exist between 800 and 1400 K. In these models, dynamical mixing brings the atmosphere out of equilibrium, resulting in relatively high abundances of parent species like ammonia and methane. At higher effective temperatures, a larger part of the atmosphere remains in chemical equilibrium, and parent species have lower concentrations, so photochemical products are less easily formed. At lower effective temperatures than ~ 800 K, parent species are plentifully available, but the UV flux is lower, owing to the larger orbital separation, so photochemistry is less effective. The UV irradiance is not the only factor, however, because the F-host simulation of 400 K receives about the same UV irradiance as the G/K-host simulations of 1000 K (Fig. 3), without showing similarly high abundances of HCN and C_2H_2. Rather, in the 400 K F-host model, production of CO and CO_2 is observed above the quench point, demonstrating that the effective temperature is still a major factor influencing the chemical composition (see also Moses et al. 2021).

The host-star type's effect on the chemical composition was mainly attributed to rotation and heat redistribution in Baeyens et al. (2021). Here, additionally the UV flux becomes an important parameter depending on the stellar host. In fact, a slight enhancement of photochemical processes is to be expected in our simulations as the stellar type changes from M to G, with a bigger jump for the F-types (Miguel & Kaltenegger 2014, and Fig. 3). Such a trend seems to be present indeed, with the F-type models consistently showing signs of molecular dissociation at greater depths than the other simulations with equal effective temperature (Figs 4 and 5). However, due to the inherent scatter in stellar XUV fluxes (see also Section 2.3), this trend can be viewed as a demonstration of the possible diversity in, rather than a strictly monotonous relationship of stellar type with, irradiation-driven photochemistry.

Finally, in the hot atmosphere simulations, the strong UV flux causes large parts of the upper day-side atmosphere to be depleted in CO and H_2O. In our isothermal upper atmosphere, which may not be a good assumption for these ultra-hot models (e.g. Lothringer et al. 2018; Arcangeli et al. 2018; Parmentier et al. 2018) or in general (see Section 4.2), most water is destroyed at the day side at pressures lower than 10^{-4} bar, and CO at pressures lower than 10^{-6} bar. This photolysis comes on top of the thermal dissociation that is expected in ultra-hot Jupiters (e.g. Parmentier et al. 2018). At the night side, on the other hand, the atomic constituents recombine into CO and H_2O. As such, photolysis of H_2O could exacerbate thermally driven limb asymmetries in ultra-hot exoplanets. Furthermore, molecular dissociation and recombination have been shown to affect the planetary heat redistribution (Bell & Cowan 2018; Tan & Komacek 2019; Roth et al. 2021) and potentially bias retrievals (Pluriel et al. 2020). It could therefore be worthwhile to take into account both thermal and photochemical dissociations when studying ultra-hot Jupiters, as was already indicated by Shulyak et al. (2020).

3.2 The Effect of Gravity

The influence of gravity on two-dimensional photochemistry is investigated by running pseudo-2D chemical kinetics models corresponding to three different values of the planet's gravity, namely 1 m/s^2, 10 m/s^2, and 100 m/s^2. The other parameters of the simulation are an effective temperature of 1200 K and a K5-star host. The configuration with 10 m/s^2 is comparable to the hot Jupiter HD 189733 b. The necessary input data, such as temperature structures and vertical mixing efficiencies, are adopted from the GCMs
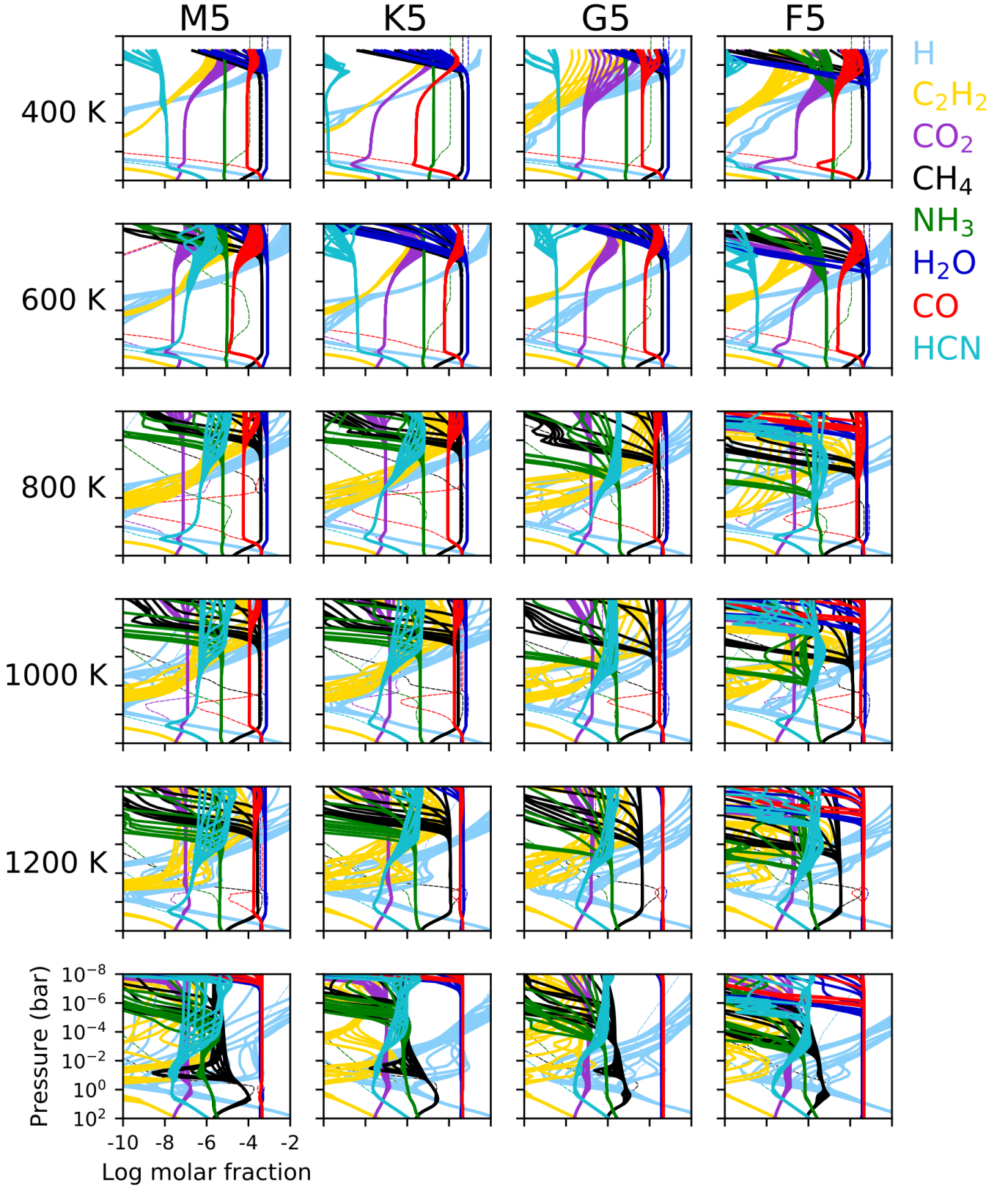
Figure 4. The cool (400–1400 K) photochemical models in our grid show strong photolysis in the upper atmosphere, with substantial number fractions of acetylene (C_2H_2). For each species (see colour legend), twelve profiles are plotted, corresponding to longitudes -180°, -150°, ..., 150°. The dashed lines show the chemical equilibrium composition at the substellar point for comparison.
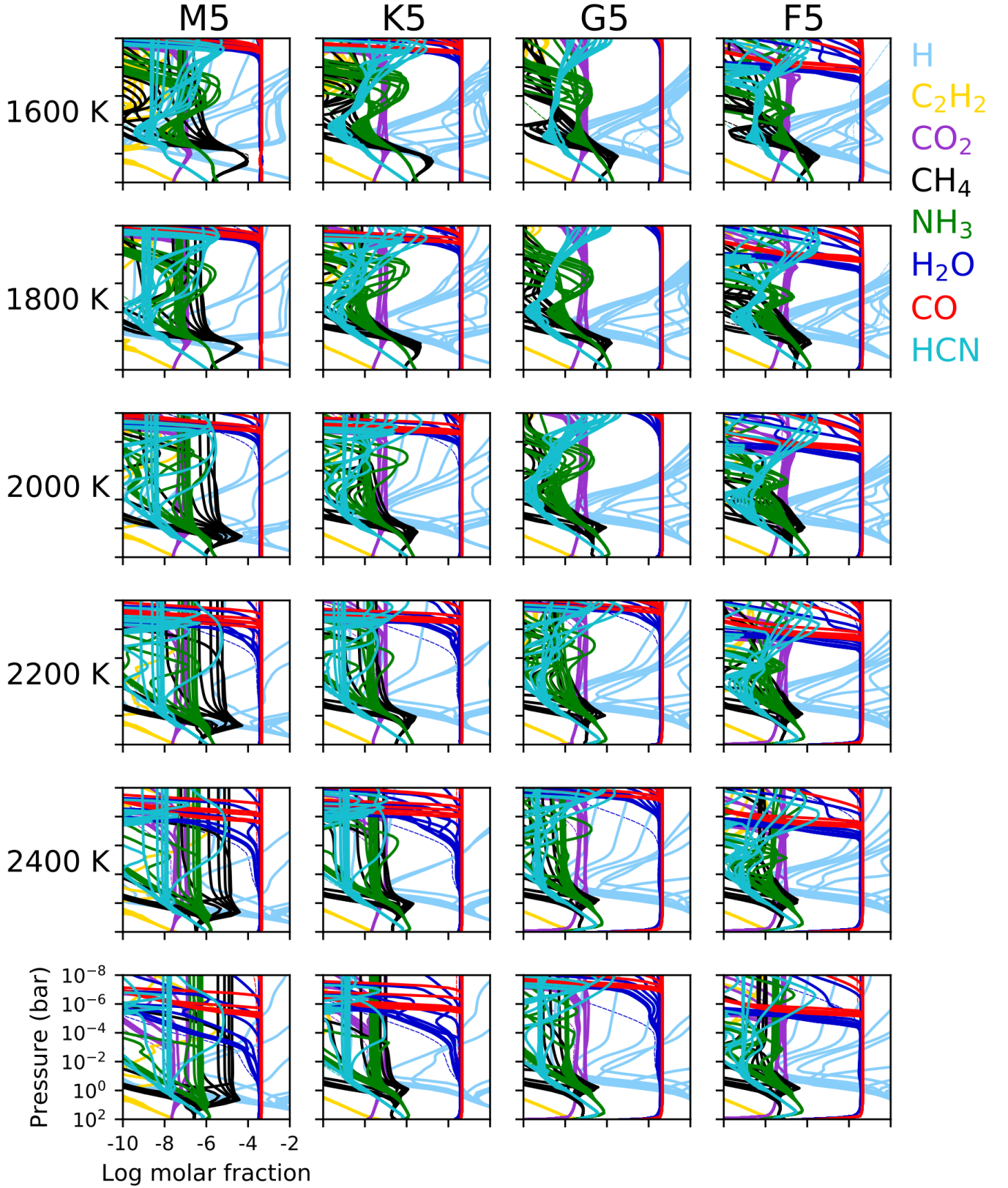
Figure 5. The hot (1600–2600 K) photochemical models in our grid have molecular number fractions that vary strongly with pressure and longitude. For each species (see colour legend), twelve profiles are plotted, corresponding to longitudes -180°, -150°, ..., 150°. The dashed lines show the chemical equilibrium composition at the substellar point for comparison.
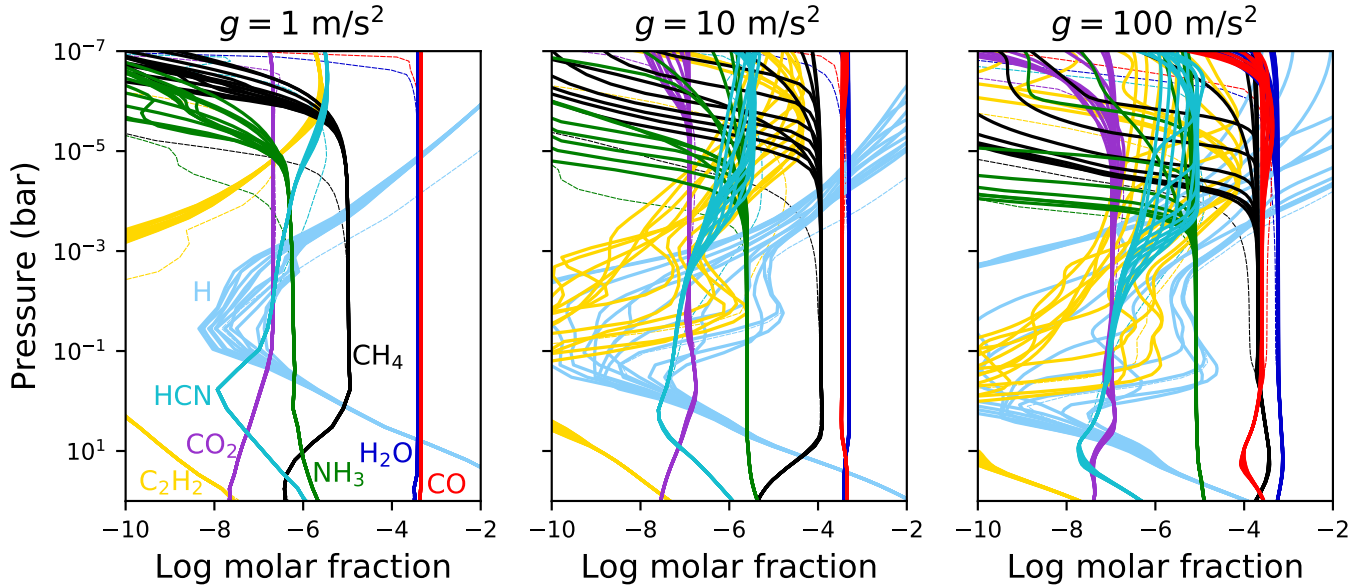
Figure 6. Upon comparing the chemical composition of a 1200 K-simulation with K5-host star and three different values for the gravity: 1 m/s^2 (*left*), 10 m/s^2 (*middle*), and 100 m/s^2 (*right*), we find that a higher gravity results in a generally increased impact of photochemistry. This is exemplified by dissociation of CH$_4$ and NH$_3$ at higher pressures, and increased horizontal gradients of H and C$_2$H$_2$. Chemical species are plotted at longitudes -180°, -150°, . . . , 150°, and colour coded the same way as Figs 4 and 5.

of Baeyens et al. (2021). As such, they are being self-consistently varied together with the gravity in order to obtain physically realistic simulations. In the models of Baeyens et al. (2021), the gravity is changed by varying the mass while keeping the radius fixed.

The three models with different gravity show clear changes in the pressure level that corresponds to the onset of photochemical dissociation (Fig. 6). In the low-gravity model, ammonia and methane get dissociated at pressures of 10^{-5} bar or lower. In the high-gravity case, on the other hand, photodissociation already affects the chemical composition at pressures slightly lower than 1 mbar. These differences are partly due to the underlying discrepancies in thermal structure and mixing efficiency. Additionally, this phenomenon is explained when considering the optical depth as a function of pressure $\tau_\nu(p)$ in a hydrostatic atmosphere. This quantity is computed as

$$\tau_\nu(p) = \int_p^0 \frac{\kappa_\nu}{g} \mathrm{d}p',$$ (1)

where κ_ν is the opacity per unit mass. We note that, since the opacity depends on the chemical composition and thermodynamic state of the atmosphere, it also depends on the gravity itself. So equation (1) is weakly non-linear in gravity. Nevertheless, for comparable atmospheric structures with different gravity, the factor g in (1) dominates (e.g. see Fortney 2018).

Thus, for a high-gravity planet, the optical depth becomes comparatively small and radiation will be able to penetrate to larger pressures. As such, high-gravity planets are more affected by photochemical processes. Given the relatively high gravity of HD 189733 b itself (g = 22 m/s^2), it is conceivable that photochemical dissociation plays a role in the non-detection of methane in this planet via high-resolution spectroscopy (Brogi et al. 2018). However, a more tailored modelling effort of the high-resolution spectrum of HD 189733 b would be necessary to verify this hypothesis.

An additional result of the increased photochemistry at high

pressures in the case of high gravity are the elevated abundances of acetylene and atomic hydrogen. These two species both attain molar fractions higher than 10^{-6} in the 1 – 100 mbar range, on the day-side of medium- and high-gravity planets (Fig. 6). In these cases, acetylene could be sufficiently abundant to enable its detection with the *James Webb Space Telescope* (Gasman et al. 2022). The low-gravity model, however, only contains appreciable fractional abundances of C$_2$H$_2$ and H in the upper part of the atmosphere ($p < 1$ mbar).

3.3 Synthetic Spectrum

To quantify the observational impact of photochemistry, we have computed synthetic transmission spectra for each model with the radiative transfer code *petitRADTRANS* (Mollière et al. 2019). We have used the same approach as in Baeyens et al. (2021), namely computing the transmission spectrum for the morning and evening limbs separately, and then averaging the squared results. The line opacities used in the spectral synthesis are H$_2$, C$_2$H$_2$ (Rothman et al. 2013), O, O$_2$ (Gordon et al. 2017), C$_2$H$_4$ (Mant et al. 2018), H$_2$O, CO, CO$_2$, OH (Rothman et al. 2010), CH$_4$ (Yurchenko & Tennyson 2014), NH$_3$ (Yurchenko et al. 2011) and HCN (Harris et al. 2006; Barber et al. 2014). For additional details, we refer to Baeyens et al. (2021) for the model setup, and Mollière et al. (2019) for the code.

The effect of photochemistry on transmission spectra is relatively subtle for cool planets ($T_{\text{eff}} \leq 1400$ K, Fig. 7), and practically negligible for hot planets (not shown here), when low-to-medium resolution transmission spectroscopy from the *Hubble* or *James Webb Space Telescopes* is considered. Although we have shown that the impact of photochemistry on the chemical abundances is considerable, the transmission signature is formed near 10-100 mbar. These pressures are too high to experience the substantial photolysis of the upper atmosphere (Fig. 4). The photochemical acetylene production at these pressures is probably also insufficient to be detectable in transmission.

HCN thus appears to be the most promising observable sig-
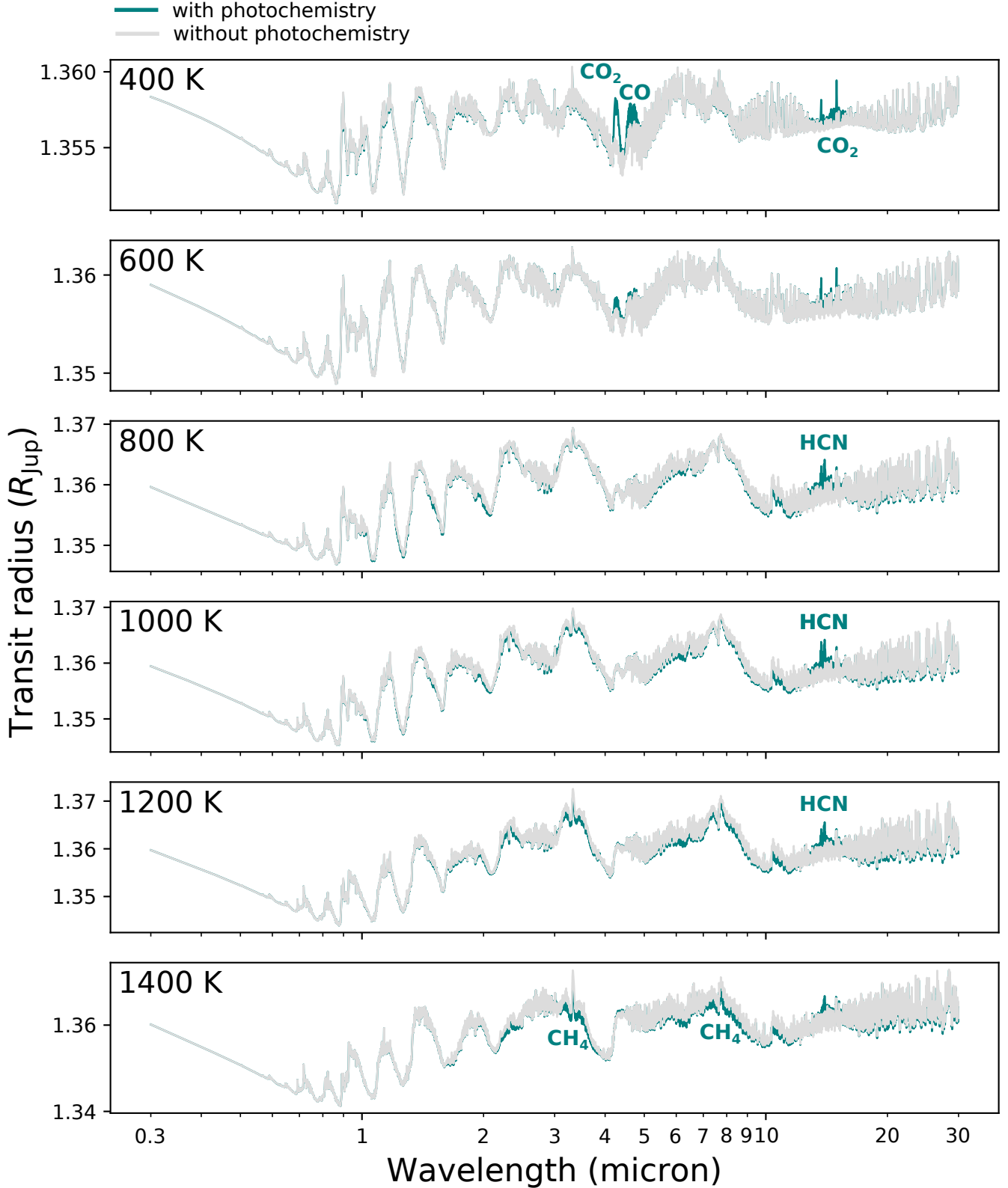
Figure 7. The synthetic transmission spectra computed with *petitRADTRANS*, corresponding to cool atmospheres with F-star hosts, show only small differences when photochemistry is included (*teal*) or not (*light grey*). Still, around 14 micron, increased HCN absorption can be seen, as well as CO and CO_2 absorption in the coldest models. In the warm ($\sim$1400 K) models, a reduced opacity caused by CH_4-dissociation is noticeable as well. Note that the vertical axes are scaled differently.

nature of photochemistry. Especially in the effective temperature region of 800–1200 K, which we identified as a sweet spot for photochemistry earlier, HCN shows a prominent absorption signature at 14 μm, in the same wavelength region where acetylene shows a strong opacity spike. The HCN spectral profile is also broader than the narrow C_2H_2 absorption. The signature of HCN, potentially combined with acetylene, can thus result in transit depth differences of ~ 70–100 ppm in our models with F- and G-star hosts (Fig. 7). The atmospheric chemistry for planets around different host stars is comparable (Figs 4 and 5), so a relatively small host star will be the most favourable to obtain a large transmission signature. Indeed, the difference in transit radius between the model spectra with and without photochemistry would result in a detectable transit depth difference of 1000 ppm for M-star hosts.

Another possible photochemistry signature arising from our synthetic transmission spectra, are the surprisingly large quantities of CO and CO_2 present in the 400 K models. This results in prominent opacity bumps for both species in the 4.3–4.6 μm wavelength range, as well as around 15 μm for CO_2. In our models, photochemical enhancements of CO and CO_2 can give rise to a transit depth that is up to 100 ppm larger than when photochemistry is ignored. Photochemistry of CO and CO_2 has been studied before (Line et al. 2011; Moses 2014), but not for effective temperatures as cold as 400 K and for strong UV irradiation.

Finally, we note that photochemistry can give rise to a decrease in CH_4 through photolysis in the 1200–1400 K range (Fig. 7), as well as modest middle-atmosphere enhancements of NH_3 in the 1600–1800 K range (Fig. 5). Our synthetic observations suggest that such differences could give rise to 50–150 ppm changes in transmission spectroscopy. However, given the broad transmission signatures of methane and ammonia, we argue that such photochemical influences would be very degenerate with changes to the metallicity, C/O ratio, or K_{zz}, all of which can affect the abundances of methane and ammonia in this temperature regime (see e.g. Venot et al. 2014). A higher C/O ratio in particular would result in more HCN and C_2H_2 production (Venot et al. 2015), similar to what is expected from photochemistry.

We note that in this work we have focused on the analysis of exoplanet observations using transmission spectra rather than emission spectra or phase curves (Moses et al. 2021), because of two reasons. First, the climate models underlying our chemistry simulations have been performed using parametrized radiative forcing. Thus, the climate models lack a self-consistent energy budget, making this method not ideal for the quantitative synthesis of emission spectra (see also the discussions on Newtonian cooling in Showman et al. 2020; Baeyens et al. 2021; Schneider et al. 2022). Second, we expect the effect of photochemistry to be more prominent in transmission spectra, because generally higher altitudes are probed (10 – 100 mbar, compared to 10 mbar – 10 bar for emission spectra). While it could be conceived that emission spectra at eclipse phase are especially sensitive to photochemistry, given their origin from the planetary day-side, we expect efficient horizontal mixing to skew the whole atmosphere toward the day-side composition anyway (see Agúndez et al. 2014a; Baeyens et al. 2021, and Section 4.1).

4 DISCUSSION

4.1 Photochemistry in the Deep Atmosphere and Night Side

That photochemistry affects the upper atmospheric day side, is evident. However, dynamical mixing processes can transport products

of photolysis to the deep atmosphere, or to the night side, thereby affecting the chemical composition as a whole. By subtracting the abundances of simulations with and without photochemistry, but using an otherwise equivalent setup, the wider impact of day-side irradiance on the planetary atmosphere is gauged.

The depth at which photochemistry starts to have a strong impact on the chemical composition, appears to decrease with effective temperature (Fig. 8). In cold models, atmospheric layers at 4 bar already experience strongly increased acetylene and atomic hydrogen concentrations. This maximal pressure of influence for photochemistry is reduced to 10^{-2} bar for intermediate temperatures (T_{eff} = 1600 K), and even 10^{-4} bar for the hottest case, ignoring the consistent night-side enhancement of acetylene here[4]. Although the UV irradiance increases strongly with effective temperature (Fig. 3), it appears that the high day-side temperature of hot atmospheres gives rise to fast chemical reactions and efficient recombination of photolysed species. Hence, the atmosphere does not go out of chemical equilibrium.

Indirectly, photochemistry also affects the night-side composition, as the species that have been formed through photochemical processes on the day side of the planet are advected via the horizontal jet stream. Especially cool planets exhibit such efficient horizontal advection, as evidenced by the roughly coinciding abundances of photochemically produced species at the day side and night side of the planet (Fig. 8, H, C_2H_2, CO, and CO_2 for T_{eff} = 400–600 K; HCN and C_2H_2 for T_{eff} = 800–1600 K). The efficient day-night transport of photochemically produced species is in agreement with our finding that cool planets tend to be horizontally homogeneous, and globally evolve towards the day-side composition (Baeyens et al. 2021).

Species that are destroyed through photolysis on the day side also get advected towards the night side of the planet, resulting in moderate night-side depletions of ammonia and methane for effective temperatures between 800 and 1800 K (Fig. 8). However, in these cases, day-side depletion is much more pronounced, which indicates that, by the time methane- and ammonia-deficient air is advected, some photochemistry products have already been recycled into NH_3 and CH_4. The partial replenishment of NH_3 and CH_4 after it has been destroyed through photolysis at the planetary day side can be attributed to vertical mixing. Indeed, an additional simulation without vertical mixing demonstrates that the night-side abundances of ammonia and methane remain low, despite them being thermochemically favoured here. The gradual replenishment of photodissociated species, as gas is advected across the night side of the planet, further implies that the morning and evening terminator have different compositions, with the latter being more depleted in ammonia and methane (see also Fig. 4).

Regarding exoplanet atmospheres with effective temperatures above 1800 K, our models suggest that photochemically enhanced or depleted species display discrepant concentrations on the day side and night side (Fig. 8), indicating that thermal effects dominate over horizontal advection. This is likely exacerbated when a temperature inversion or a hot thermosphere (Section 4.2) is taken into account.

We note that our model only takes into account horizontal advection in the eastward direction along the equator. Previous climate simulations (e.g. Rauscher & Kempton 2014; Carone et al. 2020;

---

[4] Note that, although the night side of hot photochemical simulations appears strongly enhanced in C_2H_2, its concentration is still very low in absolute terms. In the 2600 K model, the molar fraction of C_2H_2 increases from 10^{-22} to 10^{-14} when photochemistry is included.
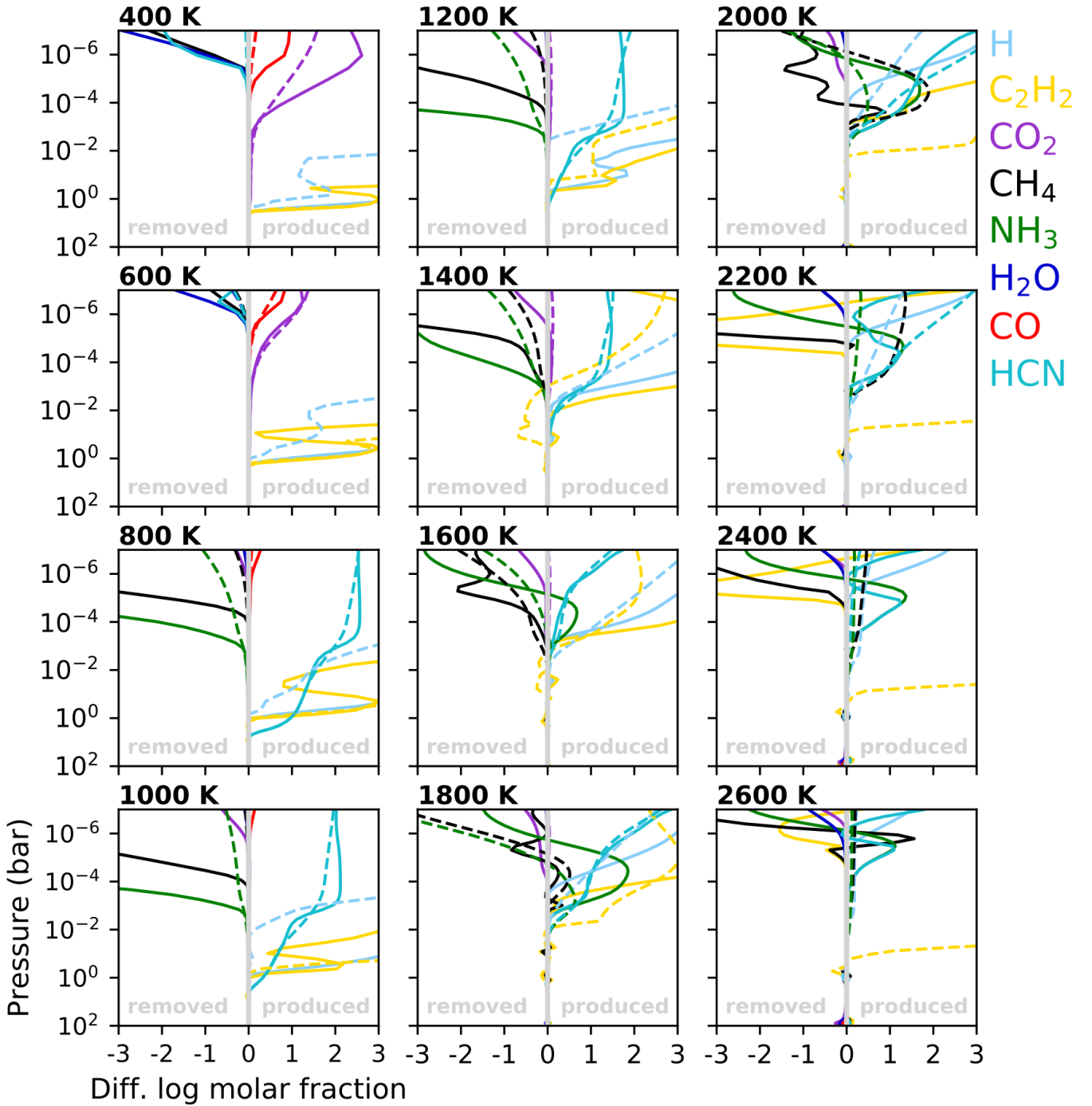
Figure 8. The difference between pseudo-2D photochemical models with photochemistry and without photochemistry, for the cases with $g = 10$ m/s^2 and a G5-host, indicates the depth up to which photochemical processes change the atmospheric composition. For each species, the differential abundance at substellar (*full*) and antistellar point (*dashed*) are shown. A positive difference indicates a higher abundance of a species in the photochemical kinetics model.

Steinrueck et al. 2021; Baeyens et al. 2021) have demonstrated that the predominant wind direction at high altitudes is a direct day-to-night flow. Thus, it would be interesting to investigate whether such wind advection would increase the transport of photochemically produced species towards the night side. This would require a 3D chemistry-coupled GCM with photochemistry, which as of yet has not been developed for hot Jupiters.

4.2 Upper Atmosphere Temperature

Theoretical models for the upper atmospheres ($p < 10^{-6}$ bar) of hot Jupiters have suggested that strong irradiation and ionization cause the temperature to rise again, reaching values of up to 10000 K in the upper thermosphere (Yelle 2004; García Muñoz 2007; Koskinen et al. 2013). Similar trends have been confirmed by detections of the atomic line profiles of sodium, formed high in the atmospheres

of hot Jupiters (Vidal-Madjar et al. 2011; Huitson et al. 2012; Pino et al. 2018). Therefore, our simple assumption of an isothermal extension of the pressure-temperature profiles is not expected to hold up to the upper boundary of $p = 10^{-8}$ bar. In order to gauge the sensitivity of our results to the upper atmospheric thermal structure, we investigate the chemical composition for a higher background temperature in the upper atmosphere.

We run our photochemical model again for typical hot Jupiter values (T_{eff} = 1400 K, g = 10 m/s^2, G5-star host), but with a hotter upper atmosphere. Instead of an isothermal extension for layers above 10^{-4} bar, we employ a parametrized thermosphere, constructed as follows. The pressure-temperature profiles are still derived from the GCM models in Baeyens et al. (2021), and isothermally extended for pressures between 10^{-4}–10^{-6} bar, but for higher pressures we perform a logarithmic interpolation to an upper boundary temperature of 5000 K at 10^{-8} bar. This upper boundary temperature is further weighted with $\cos \lambda$, where λ is the longitude with substellar point at $0°$, so that only the day side is affected, and there is a smoother transition to the isothermal night side. While this is a crude parametrization of thermospheric heating, it should be sufficient to investigate the impact of the upper atmosphere temperature structure on the chemical composition in the layers below.

From a comparison between a 1400 K-model with an isothermal photosphere, and one with parametrized thermospheric heating, we find that differences are generally restricted to pressures lower than 10^{-6} bar, i.e. the region where the heating is implemented (Fig. 9). Most notably different, the model with a hot thermosphere displays strong thermal dissociation of CO, HCN, and water in the uppermost layers at the day side of the atmosphere. However, at the night side, where no thermospheric heating is assumed, the chemical composition is unaffected. We notice a small effect of a hot thermosphere on lower lying layers, namely a slightly higher acetylene abundance, mostly on the night side of the planet (Fig. 9). In absolute values, however, the acetylene concentration is not strongly affected.

Thus, we conclude that thermospheric heating only has a minor influence on composition at intermediate or high atmospheric pressures ($p < 10^{-4}$ bar). The regions where the heating takes place ($p < 10^{-6}$ bar), however, are markedly changed. Hence, our simple assumption of an isothermal extension of the pressure-temperature profiles into the upper atmosphere is valid for the purposes of this study. A similar conclusion was reached by Moses et al. (2011), and we confirm it here in a pseudo-2D framework.

4.3 Comparison to Earlier Works

In their one-dimensional chemical kinetics study, Moses et al. (2011) raised the question whether horizontal quenching could lead to the reconversion of photochemically produced species (HCN, C_2H_2, and H) back into their parent species (NH_3, CH_4, and H_2 respectively) on the terminators or night side of irradiated planets. Using pseudo-2D models including photochemistry, it was found that HCN remains stable in high quantities after advection to the night side in hot Jupiter atmospheres of 1200–1400 K (Agúndez et al. 2014a; Venot et al. 2020b). In these models, HCN shows little to no horizontal variations, except at high altitudes ($p < 10^{-4}$ bar). Furthermore, a qualitatively similar conclusion was reached for a suite of Neptune-sized exoplanet models (Moses et al. 2021). These authors also examined different effective temperatures, and found that acetylene and HCN remain horizontally quenched in cool atmospheres, up until ~1100 K and ~1500 K respectively. This is in good qualitative agreement with our findings of strong photo-

chemical contamination of the night side at low effective temperatures, although we obtain more zonal variation in the abundance of acetylene. Additionally, our models demonstrate a higher zonal variation for planets around lower-mass stars (e.g. compare HCN in the 1400 K, M5-, K5-, G5-models, Fig. 4), because planets around cooler stars rotate faster and experience a higher day-night temperature contrast, with slower and narrower horizontal wind jets (Baeyens et al. 2021). A comparatively high XUV irradiance, however, can counteract this effect (F5-models, Fig. 4).

Shulyak et al. (2020) have examined the impact of stellar irradiation on the exoplanet atmospheric chemistry in a 1D context, and have found a strong impact of photochemistry in hot stars (A0, F0) relative to cool stars (G2, K0). The authors suggest that disequilibrium chemistry can be detected in transmission spectra of 1000 K planets, through enhanced CO, CO_2, and HCN concentrations, but becomes undetectable in models of 2000 K. In this work, with a finer effective temperature grid and pseudo-2D chemistry, we find that HCN is best observed in the 800–1200 K temperature range, in agreement with Shulyak et al. (2020), although our HCN mixing ratio and transmission signal are somewhat lower. This can be attributed to a different thermal structure, K_{zz}-profile, or (for altitudes above $p = 10^{-2}$ bar) reduced HCN concentrations at the terminators in the pseudo-2D configuration. The enhanced CO and CO_2 abundances found by Shulyak et al. (2020) have also been addressed by Blumenthal et al. (2018) as a good indicator of disequilibrium chemistry around 4.5 μm in the 700–800 K effective temperature range. The additional absorption appears to stem mostly from vertical mixing, as highlighted in Baeyens et al. (2021) (Section 5.4) and in atmospheric retrievals (Kawashima & Min 2021). Here, we additionally find a photochemical enhancement below effective temperatures of 600 K (Fig. 7), reconfirming the wavelength region around 4.5 μm as a spectral region of interest in future transmission spectroscopy studies, such as those with the *James Webb Space Telescope* (*JWST*).

Finally, Hu (2021) has investigated in detail the chemistry occurring in cold to temperate (T_{eff} < 300 K) gas planets. Here, an effect of the stellar type was identified through a low ammonia mixing ratio in the middle atmosphere (0.1–10 mbar) of planets orbiting K- and G-type stars, whereas M-stars allow for a higher ammonia content. A possible explanation is the reduced UV radiation of M-stars compared to their hotter counterparts (Hu 2021). We do not find such effect in our coldest, 400 K-models, which all yield similar NH_3 abundances in the middle atmosphere. An additional outcome of the models by Hu (2021) are CO and CO_2 as the most important photochemical products in cold environments where photolysis of ammonia is not taking place. This is likewise seen in our 400 K- and 600 K-models (Fig. 4), where photolysis of CH_4 and H_2O results in increased CO abundances. If NH_3 gets dissociated, an increased HCN abundance can be found as well. Additionally, we have highlighted the potential impact of CO and CO_2 on transmission spectra of cold planets (Fig. 7).

We note that for most of the works discussed here direct quantitative comparisons with our models are not straightforward due to different input physics. Potential sources for discrepancies include the temperature structure, vertical mixing, condensation, horizontal advection, and irradiation power. Thus, benchmarking efforts between different chemical models would be useful to reveal quantitative disagreements between different modelling tools.
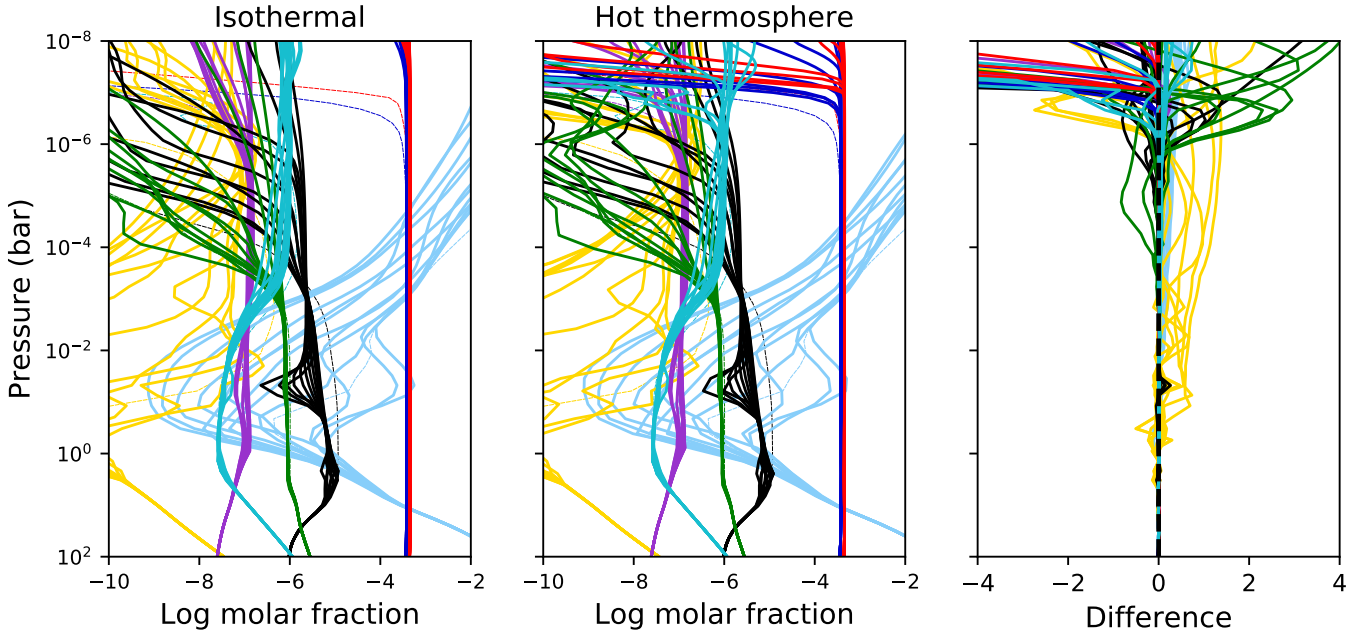
Figure 9. Our photochemical model (T_{eff} = 1400 K, g = 10 m/s^2, and G5-host) that has an isothermally extended upper atmosphere (*left*), and an equivalent photochemical model that has a hot thermosphere (*middle*), are subtracted to illustrate the abundance differences (*right*). The major differences are restricted to the upper atmosphere at pressures lower than 10^{-6} bar. Chemical species are plotted at longitudes -180°, -150°, ..., 150°, and colour coded the same way as Figs 4 and 5.

4.4 Implications for High-Resolution Spectroscopy

In Section 3.3, we have demonstrated the effect of photochemistry on the transmission spectra of irradiated exoplanets, which turns out to be limited. The reason is that photochemistry mostly affects the upper atmosphere, whereas the transmission spectrum is formed in the middle atmosphere at about 10–100 mbar. The HCN/C_2H_2 absorption peak around 14 μm is therefore one of the only signatures of photochemistry in transit spectroscopy. Unfortunately, this signal will be difficult to detect as well, as it falls outside of the wavelength range of the *JWST*/MIRI low-resolution mode[5].

Potentially, high-resolution spectroscopy of exoplanet atmospheres (e.g. Snellen et al. 2010; Birkby 2018) could be very valuable for providing constraints on photochemical processes, and vice-versa. The technique is namely sensitive to the mid- to upper atmosphere, depending on the strength of the spectral lines measured. Indeed, detections of HCN indicate its presence in the upper atmosphere of the hot Jupiters HD 209458 b (T_{eff} = 1400 K, G-type host) and HD 189733 b (T_{eff} = 1200 K, K-type host) in relatively high amounts (Hawker et al. 2018; Cabot et al. 2019). These measurements suggest a lower limit of $10^{-6.5}$ for the concentration of HCN. Such a limit is compatible with our pseudo-2D models at around 1 mbar or lower pressures (Fig. 4), assuming a solar metallicity and C/O ratio. However, additional detected molecules in the atmosphere of HD 209458 b have provided evidence of a high C/O ratio (Giacobbe et al. 2021). Likewise, a depletion of water with respect to CO in another hot Jupiter, has led to the same conclusion of a high C/O ratio (Pelletier et al. 2021). Both of these studies rely on the assumption of chemical equilibrium to infer high C/O ratios.

However, we have shown here and in Baeyens et al. (2021) how disequilibrium chemistry can affect the atmospheric composition. In particular, photolysis of water at high altitudes could potentially play a role in explaining the water depletion. This motivates further investigation expanding the parameter space of chemical kinetics models to different metallicities and C/O ratios (see also Moses et al. 2013a, 2021).

Recently, it has also become possible for high-resolution spectroscopy to probe thermal and chemical gradients in exoplanet atmospheres, such as day-night or limb asymmetries (Ehrenreich et al. 2020; Kesseli & Snellen 2021; Wardenier et al. 2021). Such effects cannot be adequately captured via one-dimensional photochemical kinetics. Thus, 2D or 3D models that include photochemistry will remain uniquely useful tools in the interpretation and prediction of the spatial distribution of molecular species at high altitudes.

4.5 Acetylene and Haze Formation

Acetylene (C_2H_2) is a commonly detected molecule in the Solar System gas giants, with an abundance following the solar insolation (e.g. Guerlet et al. 2009; Giles et al. 2021). Recent development of a high-temperature line list (Chubb et al. 2020) has enabled its detection in a hot Jupiter atmosphere as well (Giacobbe et al. 2021). We identified a sweet spot of acetylene formation in exoplanet atmospheres between 800 and 1400 K (Section 3). In this temperature range, acetylene can attain molar fractions higher than 10^{-7} in the mid- to upper atmosphere ($p < 10$ mbar). At these molar fractions, it could be detected with retrieval modelling of *JWST* data (Gasman et al. 2022). As mentioned in Section 3.3, efforts of detecting acetylene with transmission spectroscopy will likely be hampered, however, due to the decreasing abundance of acetylene at higher pressures.

With acetylene being a photochemical haze precursor molecule

---

[5] Although the *JWST*/MIRI medium-resolution observing mode (MRS) will have a wavelength range of up to 28 μm, this mode will not be suitable for transmission spectroscopy due to read-out constraints.

(Zahnle et al. 2009a), we hypothesize that the 800–1400 K temperature region could also be a sweet spot for the efficient formation of photochemical hazes in exoplanet atmospheres. Gao et al. (2020) have predicted that hydrocarbon hazes could be the dominant aerosol opacity source in the atmospheres of planets with equilibrium temperatures below 950 K (down to 700 K, the lower limit in their study). They find that haze formation becomes efficient when the atmosphere transitions from CO-dominated to CH_4-dominated, a requirement that has been formulated before by Liang et al. (2004). The transition temperature of 950 K is based on thermochemical equilibrium models. However, we have shown that appreciable methane concentrations can persist up until 1400 K with disequilibrium chemistry (Fig. 4), so potentially, photochemical hazes follow this trend. Indeed, photochemical microphysics models (Lavvas & Koskinen 2017; Helling et al. 2020) have demonstrated the potential for haze formation in HD 189733 b and WASP-43 b, which have equilibrium temperatures of 1200 K and 1400 K respectively. Thus, even though haze production is expected to slow down at higher temperatures (Kawashima & Ikoma 2019), it appears that the relatively efficient acetylene production in our photochemical models corresponds to the temperature range in which haze formation can be expected.

Finally, we note that laboratory experiments at 800 K have demonstrated that photochemical haze formation does not necessitate methane photolysis (He et al. 2020), and depends strongly on the initial mixture and atmospheric influences. Additional physics, such as ionizing radiation of stellar or cosmic origin, may also enhance the hydrocarbon concentration and facilitate haze production (Rimmer et al. 2014; Barth et al. 2021). It is clear that more sophisticated models, coupling disequilibrium chemistry, microphysics and radiative feedback, are necessary to pin down the exact dependencies of photochemical haze formation in exoplanet atmospheres.

5 CONCLUSIONS

In this study, we have investigated photochemistry in a suite of irradiated exoplanet atmospheres in order to gauge its impact on the atmospheric composition and on transmission spectra. To achieve this, we have used the pseudo-2D chemical kinetics code of Agúndez et al. (2014a) with the full chemical network of Venot et al. (2020a), and updated our grid of models for irradiated exoplanet atmospheres by extending them to higher altitudes and including photochemistry.

In our photochemical models, we find that the upper atmospheres are depleted in CH_4 and NH_3, and for high UV irradiance also H_2O and CO. On the other hand, in the middle atmosphere, HCN and C_2H_2 are being produced from photolysed ammonia and methane in cool planetary atmospheres. The maximal pressure at which photochemical processes affect the chemical composition, decreases with effective temperature, and is about 4 bar in the coolest planet. Furthermore, we identify a sweet spot for the photochemical production of C_2H_2 and HCN between 800 K and 1400 K, and discuss the potential for photochemical haze formation in this temperature region.

Our models suggest an efficient longitudinal transport for effective temperatures below 1800 K, with a strong contamination of the night side by photochemically produced species from the day side, in agreement with other pseudo-2D models (Agúndez et al. 2014a; Venot et al. 2020b; Moses et al. 2021). Photolysed ammonia and methane, however, are partially replenished on their way to the night side, suggesting a zonal chemical gradient with limb asymmetries.

The impact of the host star on the chemical composition asserts itself mostly through the changing UV irradiance. In our models, photochemical processes are enhanced when the host star temperature increases, in agreement with Shulyak et al. (2020). However, we note that this trend not necessarily applies universally, due to the large intrinsic scatter in stellar X-ray and UV luminosities (Linsky et al. 2020). Hence, future work continuing to quantify the spread of XUV luminosities of exoplanet host stars, as well as the corresponding variations that can be expected for planetary atmospheric photochemistry, would be very beneficial.

Despite the considerable impact of photochemistry on the atmospheric composition, the impact on transmission spectra was found to be feeble for planets with effective temperatures below 1400 K, and nearly negligible for planets with higher effective temperatures. The most prominent signature of photochemistry in transmission, is the enhanced absorption at 14 μm, but it will be difficult to detect, as it lies outside the wavelength range of the *JWST*/MIRI stable, spectrophotometric observing mode. Potentially, a 50 to 150 ppm variation because of photochemically reduced methane or enhanced ammonia concentrations is detectable, although it will be degenerate with other exoplanet properties. A potentially important effect of photochemistry on transmission spectroscopy, which is, however, not probed by our chemical network is photo-ionization and the increased abundance of H^-. The latter has been shown to be an important opacity source in the hydrogen-rich atmospheres of exoplanets (Arcangeli et al. 2018; Lewis et al. 2020; Rathcke et al. 2021).

In high-resolution spectroscopy observations, which typically probe higher altitudes than transmission spectroscopy, photochemistry potentially has a bigger role to play. HCN and C_2H_2 have already been detected in some exoplanets (Hawker et al. 2018; Cabot et al. 2019; Giacobbe et al. 2021), and are being used to constrain their elemental abundances. Photochemistry, and disequilibrium chemistry in general, are important to understand such results. In addition, a pseudo-2D or 3D framework is particularly favourable to interpret the spatial distribution of chemical species at high altitudes, which can also be probed with high-resolution spectroscopy (Ehrenreich et al. 2020; Kesseli & Snellen 2021).

Finally, we note that in our models, we have adopted constant stellar spectra and discussed time-invariant, steady-state chemistry. As such we did not incorporate the effect of stellar flares, which could alter the chemical composition of exoplanet atmospheres on short to long timescales (Venot et al. 2016). We will investigate the impact of stellar flares on exoplanetary chemistry in a 2D context in an upcoming study (Konings et al., *subm.*).

DATA AVAILABILITY STATEMENT

The data underlying this article will be shared on reasonable request to the corresponding author.

REFERENCES

Agúndez M., Parmentier V., Venot O., Hersant F., Selsis F., 2014a, A&A, 564, 73

Agúndez M., Venot O., Selsis F., Iro N., 2014b, ApJ, 781, 68

Arcangeli J., et al., 2018, ApJ, 855, L30

Baeyens R., Decin L., Carone L., Venot O., Agúndez M., Mollière P., 2021, MNRAS, 505, 5603

Barber R. J., Strange J. K., Hill C., Polyansky O. L., Mellau G. C., Yurchenko S. N., Tennyson J., 2014, MNRAS, 437, 1828

Barth P., et al., 2021, MNRAS, 502, 6201

Baxter C., et al., 2021, A&A, 648, A127

Bell T. J., Cowan N. B., 2018, ApJ, 857, L20

Birkby J. L., 2018, in Deeg H. J., Belmonte J. A., eds, , Handbook of Exoplanets. Springer, Cham, p. 16, doi:10.1007/978-3-319-55333-7_16

Blumenthal S. D., Mandell A. M., Hébrard E., Batalha N. E., Cubillos P. E., Rugheimer S., Wakeford H. R., 2018, ApJ, 853, 138

Brogi M., Giacobbe P., Guilluy G., de Kok R. J., Sozzetti A., Mancini L., Bonomo A. S., 2018, A&A, 615, A16

COESA 1976, U.S. Standard Atmosphere. U.S. Government Printing Office, Washington, D.C., https://ntrs.nasa.gov/api/citations/19770009539/downloads/19770009539.pdf

Cabot S. H. C., Madhusudhan N., Hawker G. A., Gandhi S., 2019, MNRAS, 482, 4422

Carone L., et al., 2020, MNRAS, 496, 3582

Chubb K. L., Tennyson J., Yurchenko S. N., 2020, MNRAS, 493, 1531

Claire M. W., Sheets J., Cohen M., Ribas I., Meadows V. S., Catling D. C., 2012, ApJ, 757, 95

Cooper C. S., Showman A. P., 2006, ApJ, 649, 1048

Dobrijevic M., Hébrard E., Loison J. C., Hickson K. M., 2014, Icarus, 228, 324

Drummond B., Tremblin P., Baraffe I., Amundsen D. S., Mayne N. J., Venot O., Goyal J., 2016, A&A, 594, A69

Drummond B., Mayne N. J., Baraffe I., Tremblin P., Manners J., Amundsen D. S., Goyal J., Acreman D., 2018a, A&A, 612, A105

Drummond B., et al., 2018b, ApJ, 855, L31

Drummond B., Mayne N. J., Manners J., Baraffe I., Goyal J., Tremblin P., Sing D. K., Kohary K., 2018c, ApJ, 869, 28

Drummond B., et al., 2020, A&A, 636, A68

Ehrenreich D., et al., 2020, Nature, 580, 597

Fleury B., Gudipati M. S., Henderson B. L., Swain M., 2019, ApJ, 871, 158

Fleury B., Gudipati M. S., Henderson B. L., Swain M., 2020, ApJ, 899, 147

Fortney J. J., 2018, in Bozza V., Mancini L., Sozzetti A., eds, , Astrophysics of Exoplanetary Atmospheres: 2nd Advanced School on Exoplanetary Science. Springer International Publishing, Cham, pp 51–88, doi:10.1007/978-3-319-89701-1_2, https://doi.org/10.1007/978-3-319-89701-1_2

France K., Linsky J. L., Tian F., Froning C. S., Roberge A., 2012, ApJ, 750, L32

France K., et al., 2016, ApJ, 820, 89

Gao P., et al., 2020, Nature Astronomy, 4, 951

García Muñoz A., 2007, Planet. Space Sci., 55, 1426

Gasman D., Min M., Chubb K. L., 2022, arXiv e-prints, p. arXiv:2202.01151

Giacobbe P., et al., 2021, Nature, 592, 205

Giles R. S., et al., 2021, Journal of Geophysical Research (Planets), 126, e06928

Gladstone G. R., Allen M., Yung Y. L., 1996, Icarus, 119, 1

Gordon I. E., et al., 2017, J. Quant. Spectrosc. Radiative Transfer, 203, 3

Guerlet S., Fouchet T., Bézard B., Simon-Miller A. A., Michael Flasar F., 2009, Icarus, 203, 214

Guillot T., 2010, A&A, 520, A27

Harris G. J., Tennyson J., Kaminsky B. M., Pavlenko Y. V., Jones H. R. A., 2006, MNRAS, 367, 400

Hawker G. A., Madhusudhan N., Cabot S. H. C., Gandhi S., 2018, ApJ, 863, L11

He C., et al., 2018, AJ, 156, 38

He C., et al., 2020, Planet. Sci. J., 1, 51

Hébrard E., Dobrijevic M., Loison J. C., Bergeat A., Hickson K. M., Caralp F., 2013, A&A, 552, A132

Helling C., Rimmer P. B., 2019, Philosophical Transactions of the Royal Society of London Series A, 377, 20180398

Helling C., Kawashima Y., Graham V., Samra D., Chubb K. L., Min M., Waters L. B. F. M., Parmentier V., 2020, A&A, 641, A178

Hobbs R., Shorttle O., Madhusudhan N., Rimmer P., 2019, MNRAS, 487, 2242

Hobbs R., Rimmer P. B., Shorttle O., Madhusudhan N., 2021, MNRAS, 506, 3186

Hörst S. M., et al., 2018, Nature Astronomy, 2, 303

Hu R., 2021, ApJ, 921, 27

Hu R., Seager S., 2014, ApJ, 784, 63

Hubeny I., Mihalas D., 2014, Theory of Stellar Atmospheres. Princeton University Press

Huitson C. M., Sing D. K., Vidal-Madjar A., Ballester G. E., Lecavelier des Etangs A., Désert J. M., Pont F., 2012, MNRAS, 422, 2477

Husser T. O., Wende-von Berg S., Dreizler S., Homeier D., Reiners A., Barman T., Hauschildt P. H., 2013, A&A, 553, A6

Jacobson M. C., Hansson H. C., Noone K. J., Charlson R. J., 2000, Reviews of Geophysics, 38, 267

Johnstone C. P., Bartel M., Güdel M., 2021, A&A, 649, A96

Kawashima Y., Ikoma M., 2018, ApJ, 853, 7

Kawashima Y., Ikoma M., 2019, ApJ, 877, 109

Kawashima Y., Min M., 2021, A&A, 656, A90

Kesseli A. Y., Snellen I. A. G., 2021, ApJ, 908, L17

Komacek T. D., Showman A. P., Parmentier V., 2019, ApJ, 881, 152

Koskinen T. T., Harris M. J., Yelle R. V., Lavvas P., 2013, Icarus, 226, 1678

Lavvas P., Koskinen T., 2017, ApJ, 847, 32

Lavvas P., Koskinen T., Yelle R. V., 2014, ApJ, 796, 15

Lewis N. K., et al., 2020, ApJ, 902, L19

Liang M.-C., Parkinson C. D., Lee A. Y. T., Yung Y. L., Seager S., 2003, ApJ, 596, L247

Liang M.-C., Seager S., Parkinson C. D., Lee A. Y. T., Yung Y. L., 2004, ApJ, 605, L61

Line M. R., Vasisht G., Chen P., Angerhausen D., Yung Y. L., 2011, ApJ, 738, 32

Linsky J. L., et al., 2020, ApJ, 902, 3

Locci D., Petralia A., Micela G., Maggio A., Ciaravella A., Cecchi-Pestellini C., 2022, Planet. Sci. J., 3, 1

Lothringer J. D., Barman T., Koskinen T., 2018, ApJ, 866, 27

Loyd R. O. P., et al., 2016, ApJ, 824, 102

Mant B. P., Yachmenev A., Tennyson J., Yurchenko S. N., 2018, MNRAS, 478, 3220

Mendonça J. M., Tsai S.-m., Malik M., Grimm S. L., Heng K., 2018, ApJ, 869, 107

Miguel Y., Kaltenegger L., 2014, ApJ, 780, 166

Miller-Ricci Kempton E., Zahnle K., Fortney J. J., 2012, ApJ, 745, 3

Mollière P., Wardenier J. P., van Boekel R., Henning T., Molaverdikhani K., Snellen I. A. G., 2019, A&A, 627, A67

Moses J. I., 2014, Philosophical Transactions of the Royal Society of London Series A, 372, 20130073

Moses J. I., Bézard B., Lellouch E., Gladstone G. R., Feuchtgruber H., Allen M., 2000, Icarus, 143, 244

Moses J. I., et al., 2011, ApJ, 737, 15

Moses J. I., Madhusudhan N., Visscher C., Freedman R. S., 2013a, ApJ, 763, 25

Moses J. I., et al., 2013b, ApJ, 777, 34

Moses J. I., Cavalié T., Fletcher L. N., Roman M. T., 2020, Philosophical Transactions of the Royal Society of London Series A, 378, 20190477

Moses J. I., Tremblin P., Venot O., Miguel Y., 2021, Experimental Astronomy,

Panzera M. R., Tagliaferri G., Pasinetti L., Antonello E., 1999, A&A, 348, 161

Parmentier V., Showman A. P., Lian Y., 2013, A&A, 558, A91

Parmentier V., et al., 2018, A&A, 617, A110

Pelletier S., et al., 2021, AJ, 162, 73

Pino L., et al., 2018, A&A, 612, A53

Pluriel W., Zingales T., Leconte J., Parmentier V., 2020, A&A, 636, A66

Pont F., Knutson H., Gilliland R. L., Moutou C., Charbonneau D., 2008, MNRAS, 385, 109

Pont F., Sing D. K., Gibson N. P., Aigrain S., Henry G., Husnoo N., 2013, MNRAS, 432, 2917

Poppenhaeger K., Robrade J., Schmitt J. H. M. M., 2010, A&A, 515, A98

Rathcke A. D., et al., 2021, AJ, 162, 138

Rauscher E., Kempton E. M. R., 2014, ApJ, 790, 79

Ribas I., Guinan E. F., Güdel M., Audard M., 2005, ApJ, 622, 680

Rimmer P. B., Helling C., 2016, ApJS, 224, 9

Rimmer P. B., Helling C., Bilger C., 2014, International Journal of Astrobiology, 13, 173

Roth A., Drummond B., Hébrard E., Tremblin P., Goyal J., Mayne N., 2021, MNRAS, 505, 4515

Rothman L. S., et al., 2010, J. Quant. Spectrosc. Radiative Transfer, 111, 2139

Rothman L. S., et al., 2013, J. Quant. Spectrosc. Radiative Transfer, 130, 4

Roudier G. M., Swain M. R., Gudipati M. S., West R. A., Estrela R., Zellem R. T., 2021, AJ, 162, 37

Schneider A. D., Carone L., Decin L., Gråe Jørgensen U., Mollière P., Baeyens R., Kiefer S., Helling C., 2022, arXiv e-prints, p. arXiv:2202.09183

Segura A., Krelove K., Kasting J. F., Sommerlatt D., Meadows V., Crisp D., Cohen M., Mlawer E., 2003, Astrobiology, 3, 689

Showman A. P., Tan X., Parmentier V., 2020, Space Sci. Rev., 216, 139

Shulyak D., Lara L. M., Rengel M., Nèmec N. E., 2020, A&A, 639, A48

Sing D. K., et al., 2016, Nature, 529, 59

Smith R. K., Brickhouse N. S., Liedahl D. A., Raymond J. C., 2001, ApJ, 556, L91

Snellen I. A. G., de Kok R. J., de Mooij E. J. W., Albrecht S., 2010, Nature, 465, 1049

Steinrueck M. E., Parmentier V., Showman A. P., Lothringer J. D., Lupu R. E., 2019, ApJ, 880, 14

Steinrueck M. E., Showman A. P., Lavvas P., Koskinen T., Tan X., Zhang X., 2021, MNRAS, 504, 2783

Strobel D. F., 2005, Space Sci. Rev., 116, 155

Tan X., Komacek T. D., 2019, ApJ, 886, 26

Tsai S.-M., Malik M., Kitzmann D., Lyons J. R., Fateev A., Lee E., Heng K., 2021, ApJ, 923, 264

Venot O., Hébrard E., Agúndez M., Dobrijevic M., Selsis F., Hersant F., Iro N., Bounaceur R., 2012, A&A, 546, A43

Venot O., Agúndez M., Selsis F., Tessenyi M., Iro N., 2014, A&A, 562, A51

Venot O., Hébrard E., Agúndez M., Decin L., Bounaceur R., 2015, A&A, 577, A33

Venot O., Rocchetto M., Carl S., Roshni Hashim A., Decin L., 2016, ApJ, 830, 77

Venot O., Drummond B., Miguel Y., Waldmann I. P., Pascale E., Zingales T., 2018, Experimental Astronomy, 46, 101

Venot O., Cavalié T., Bounaceur R., Tremblin P., Brouillard L., Lhoussaine Ben Brahim R., 2020a, A&A, 634, A78

Venot O., et al., 2020b, ApJ, 890, 176

Vidal-Madjar A., et al., 2011, A&A, 527, A110

Walkowicz L. M., Johns-Krull C. M., Hawley S. L., 2008, ApJ, 677, 593

Wang S., Bai Y., He L., Liu J., 2020, ApJ, 902, 114

Wardenier J. P., Parmentier V., Lee E. K. H., Line M. R., Gharib-Nezhad E., 2021, MNRAS, 506, 1258

Wong A.-S., Yung Y. L., Friedson A. J., 2003, Geophys. Res. Lett., 30, 1447

Yelle R. V., 2004, Icarus, 170, 167

Youngblood A., et al., 2016, ApJ, 824, 101

Yu X., et al., 2021, Nature Astronomy, 5, 822

Yung Y. L., DeMore W. B., 1999, Photochemistry of planetary atmospheres. Oxford University Press: New York

Yung Y. L., Allen M., Pinto J. P., 1984, ApJS, 55, 465

Yurchenko S. N., Tennyson J., 2014, MNRAS, 440, 1649

Yurchenko S. N., Barber R. J., Tennyson J., 2011, MNRAS, 413, 1828

Zahnle K., Marley M. S., Fortney J. J., 2009a, arXiv e-prints, p. arXiv:0911.0728

Zahnle K., Marley M. S., Freedman R. S., Lodders K., Fortney J. J., 2009b, ApJ, 701, L20

Zahnle K., Marley M. S., Morley C. V., Moses J. I., 2016, ApJ, 824, 137

This paper has been typeset from a TeX/LaTeX file prepared by the author.